





Cite this: *Phys. Chem. Chem. Phys.*,  
2024, 26, 9940

# Exploring mechanochemistry of pharmaceutical cocrystals: effect of incident angle on molecular mixing during simulated indentations of two organic solids†

Michael Ferguson \* and Tomislav Friščić \*

The solid-state reaction of the active pharmaceutical ingredient theophylline with citric acid is a well-established example of a mechanochemical reaction, leading to a model pharmaceutical cocrystal. Here, classical force field molecular dynamics was employed to investigate the molecular mixing and structural distortion that take place on the mechanically driven indentation of a citric acid nanoparticle on a slab of crystalline theophylline. Through non-equilibrium molecular dynamics simulations, a 6 nm diameter nanoparticle of citric acid was introduced onto an open (001) surface of a theophylline crystal, varying both the angle of incidence of the nanoparticle between 15° and 90° and the indentation speed between 1 m s<sup>-1</sup> and 16 m s<sup>-1</sup>. This theoretical study enabled the evaluation of how these two parameters promote molecular mixing and overall structural deformation upon the mechanical contraction of theophylline and citric acid, both of which are important parameters underlying mechanochemical cocrystallisation. The results show that the angle of incidence plays a key role in the molecular transfer ability between the two species and in the structural disruption of the initially spherical nanoparticles. Changing the indentation speed, however, did not lead to a discernible trend in molecular mixing, highlighting the importance of the incident angle in mechanochemical events in the context of supramolecular chemistry, such as the disruption of the crystal structure and molecular transfer between molecular crystals.

Received 10th November 2023,  
Accepted 20th February 2024

DOI: 10.1039/d3cp05475f

rsc.li/pccp

## Introduction

Mechanochemical strategies, where mechanical energy is used to induce or promote chemical transformations, are one of the most attractive routes for cleaner, more efficient and sustainable synthesis of various molecular targets and functional materials.<sup>1</sup> Mechanochemistry has been demonstrated to provide access to improved reaction yields, reduced reaction times, and vast reductions in solvent use,<sup>1</sup> while also providing pathways for reactions between poorly soluble compounds<sup>2</sup> and even access to products that are otherwise unobtainable.<sup>3</sup> Mechanochemical reactions are most commonly performed in small batches using ball mills,<sup>1a</sup> but recent reports have also engaged resonant acoustic mixing<sup>4</sup> (RAM) and twin-screw extrusion<sup>5</sup> (TSE), opening the door to establishing highly scalable approaches to mechanochemistry. A wide range of

mechanochemical techniques, including ball milling,<sup>6</sup> TSE,<sup>7</sup> and RAM,<sup>8</sup> as well as mechanically activated approaches, such as accelerated aging (also known as vapour digestion)<sup>9</sup> and vapour-assisted tumbling (VAT),<sup>10</sup> have attracted particular attention in the context of the discovery and synthesis of pharmaceutical materials, such as polymorphs or cocrystals. Processes of relevance in mechanochemical cocrystallisation of pharmaceutical solids, as well as other types of organic and metal-organic materials, are likely to be the distortion or disruption of the crystal structure (*e.g.* amorphisation), formation of defects (polymorphic transformations), and molecular mixing (mass transfer). Importantly, mechanochemical processes leading to pharmaceutical cocrystals generally do not involve the cleavage of strong covalent bonds, but rather changes in molecular assembly in the solid state and surfaces, which is based on supramolecular transformations like in the recently discussed term of soft mechanochemistry.<sup>11,12</sup>

Significant attention has been directed to developing a fundamental understanding of how diverse chemical and materials transformations, including cocrystal formation, proceed under mechanochemical conditions,<sup>13</sup> with notable mechanistic knowledge acquired following the introduction of real-time *in situ* monitoring techniques by synchrotron

School of Chemistry, University of Birmingham, Edgbaston, Birmingham B15 2TT, UK. E-mail: m.ferguson.5@bham.ac.uk, t.frischic@bham.ac.uk

† Electronic supplementary information (ESI) available: Details of computational strategies, molecular transfer, connective neck, sphericity, and force development analyses. Additionally, 24 movies are supplied, one for each of the simulated indentations presented herein as well as sample input files to run a LAMMPS simulation of the system. See DOI: <https://doi.org/10.1039/d3cp05475f>



powder X-ray diffraction,<sup>14</sup> Raman spectroscopy,<sup>15,16</sup> X-ray absorption spectroscopy,<sup>17</sup> tandem Raman and fluorescence spectroscopies,<sup>18</sup> nuclear magnetic resonance (NMR) spectroscopy,<sup>19</sup> and acoustic spectroscopy.<sup>20</sup> These techniques are now set to provide a wealth of information on mechanochemical reactivity in the bulk regime but cannot yet provide insights into underlying atomic and molecular processes that drive the reactions. Indeed, studies of mechanochemical reactions of molecular materials are in many ways additionally challenging compared to transformations of ionic solids, as intermediate and/or amorphous phases are very likely to rapidly relax before or during analysis.<sup>13</sup>

Theoretical techniques provide a wide range of strategies for probing the molecular-level mechanisms of mechanochemical processes that cannot be obtained experimentally. For example, discrete element modelling has been performed to understand how the motion of the grinding media (*i.e.*, balls or screws used to transmit mechanical energy during milling or extrusion processes, respectively)<sup>21</sup> or the shape of the mechanochemical reaction vessel<sup>22</sup> affects the delivery of mechanical energy to the reaction system. Phase-field crystal theory has been utilised to investigate how mechanical energy input can reduce the energy barrier for the nucleation of nanoparticles from a homogenous solid matrix,<sup>23</sup> while analytical models have been employed to model mechanochemical reaction kinetics<sup>24</sup> and understand how ball impacts promote bulk changes in solids.<sup>25</sup> *Ab initio* methods have been employed to probe how mechanical stress leads to covalent bond cleavage.<sup>26,27</sup> Additionally, *ab initio* calculations have shown how mechanical stress alters lattice vibrations in metal azides, which subsequently induce chemical reactions.<sup>28</sup> These techniques have generated a greater understanding of mechanochemistry but generally need to sacrifice molecular-level details to study more global effects, which are more easily transferable to experimental results or dynamic information to study energetics at the atomic level. Force field molecular dynamics (MD) allows studying the molecular level processes that occur over short time periods (ns– $\mu$ s) and, in the context of mechanochemistry, has already been employed to study the effects of shear stress on various tribochemical (*i.e.*, friction-induced) transformations<sup>29</sup> as well as for exploring molecular transfer processes between crystalline organic solids upon organic particle collisions.<sup>30</sup> Such studies are performed using a direct indentation strategy, which involves using molecular walls to push two particles together until a predefined point of maximum indentation that is followed by pulling the particles apart to facilitate the analysis of molecular transfer between the species involved.

Here, we present the use of force field MD simulations to investigate the processes taking place upon the impact of an organic crystalline nanoparticle on the surface of an organic solid. Specifically, by varying the incident angle of the crystalline nanoparticle, as well as the incident speed of the nanoparticle, it was possible to observe different levels of particle distortion and molecular mixing – phenomena of critical importance for subsequent cocrystallisation. As model crystalline materials for our study, we chose citric acid (**cit**) and the active pharmaceutical ingredient (API) theophylline (**theo**),

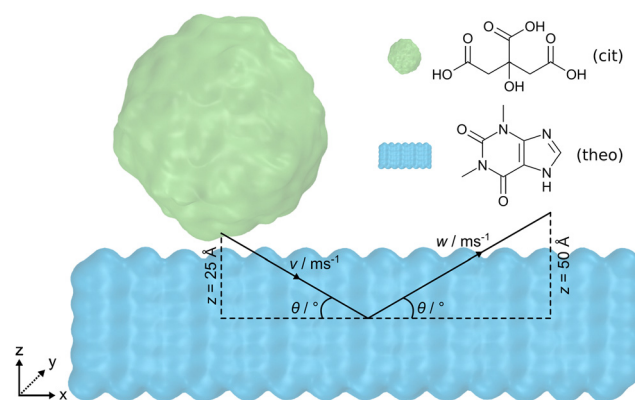


Fig. 1 Schematic representation of the simulation strategy employed in this work. A spherical nanoparticle of citric acid (green) is incident on a slab of theophylline (blue) with the (001) surface exposed. Initially separated by 5 Å, the nanoparticle travels along **v** at a given speed towards the centre of the slab until it becomes indented by 20 Å. Subsequently, the *z*-component of the atomic velocities is reversed to retract the nanoparticle from the slab along **w** at the same speed for 50 Å.

which provide relevance in the context of pharmaceutical materials science. Importantly, cocrystallisation of **theo** and **cit** acid through mechanochemical techniques has been reported by several groups, providing a model of broad significance.<sup>31</sup> In contrast to previous work where two nanoparticles were indented upon one another,<sup>30</sup> the current investigation focuses on the indentation of a spherical **cit** nanoparticle onto a flat theophylline surface (Fig. 1). By systematically reducing the incident angle from 90° to 15°, we gain insights into both the molecular transfer process and the structural deformation of the particles. Lower incident angles (15° and 30°) lead to a significant increase in the number of molecules exchanged between **cit** and **theo**, and a noticeable decrease in the sphericity of the originally spherical nanoparticles of **cit**. Additionally, the simulations reveal that the effects of the angle of incidence overshadow those of the incident speed during the presented indentations.

## Computational methods

The molecular dynamics (MD) engine LAMMPS,<sup>32</sup> v29Oct2020, was employed to simulate indentations of a **cit** nanoparticle on an open surface of a **theo** slab at various incident speeds along the vector **v** and angles  $\theta$ , as shown in Fig. 1. Upon reaching the desired indentation point, the **cit** nanoparticle was retracted from the **theo** slab along the vector **w**, at the same speed as the indentation. Interatomic interactions were described by the OPLS-AA force field<sup>33</sup> with non-bonded interactions modelled using Lennard-Jones<sup>34</sup> potentials truncated at 12 Å. Hydrogen bonding interactions were incorporated by overlaying the Lennard-Jones potentials with the angle-dependent 12-10 form, as described in the DREIDING force field.<sup>35</sup> Electrostatic interactions were calculated using the particle-particle particle-mesh (PPPM) solver<sup>36</sup> with atomic charges that were obtained from Hirshfeld charge analysis performed using the periodic density functional theory (DFT) code CASTEP, v22.11.<sup>37</sup> Crystal



structures used to model **cit** and **theo** were obtained from the Cambridge Structural Database<sup>38</sup> (CSD) with the reference codes CITRAC10<sup>39</sup> and BAPLOT01,<sup>40</sup> respectively. Full details of the DFT calculation parameters and sample input files for the MD simulations with LAMMPS can be found in the ESI.†

To obtain a size comparable to previous work<sup>36</sup> (diameter =  $\approx 6$  nm), a spherical region (radius = 30 Å) of molecules was extracted from a  $12 \times 30 \times 15$  supercell of the **cit** crystal structure. If any atom of a molecule falls within the radius, then that molecule was included as part of the nanoparticle, resulting in a final nanoparticle radius of 31.5 Å. The slab geometry for **theo** was generated by creating a  $7 \times 28 \times 5$  supercell of the pure crystal and then extending the *z*-axis by 130 Å. This allowed the **cit** nanoparticle to be positioned above the slab surface, while ensuring that there would be no interactions between the **cit** and the **theo** slab through the periodic boundary conditions. The nanoparticle and the slab were equilibrated separately for 1 ns at 300 K in the NVT ensemble and subsequently combined to produce a 97 000 atom system ready for simulated indentations. Following previous studies,<sup>30,41</sup> the motion of the objects in the presented simulations was controlled by fixing the trajectories of a small section of the molecules of each material. For **theo**, 392 molecules that formed the bottom layer of the slab were selected and their velocities were set to zero, to fix the slab in place. For **cit**, 115 molecules contained within the uppermost 15 Å of the particle were selected and used to move the nanoparticle at a given speed along *v* and *w* (Fig. S1, ESI†). Based on estimated ball speeds in a ball mills<sup>42,43</sup> of  $8 \text{ m s}^{-1}$  and  $1 \text{ m s}^{-1}$ , we decided on the set of speeds, 1, 4, 8, and  $16 \text{ m s}^{-1}$ , where  $16 \text{ m s}^{-1}$  was

chosen to overestimate the ferocity of the indentation. For the incident angle of the particle, we chose a range of  $\theta = 15^\circ$  to  $90^\circ$  with increments of  $15^\circ$ . In the case where  $\theta = 90^\circ$ , the **cit** nanoparticle was positioned so that its geometrical centre was directly above the centre of the *xy* centre of the **theo** slab and with a 5 Å separation in *z* between the two structures. The depth of the indentation in *z* of the **cit** nanoparticle to the slab was set at 20 Å; therefore, the nanoparticle will travel 25 Å in *z* to reach this point of maximum indentation. For indentations where  $\theta \neq 90^\circ$ , the **cit** particle was displaced negatively along the *x*-axis, as calculated using simple trigonometry (Section S1.1, ESI†). This ensured that the position of the **cit** particles relative to the **theo** slab at the maximum indentation was identical for each simulated indentation. Upon reaching the maximum indentation, the **cit** particle was retracted from the **theo** slab to facilitate the analysis. The nanoparticle was retracted along *w* at the same speed and retracted over a distance of 50 Å to guarantee a final configuration comprising two contiguous objects.

## Results and discussion

The analyses of the effect of the speed and incident angle are presented (Fig. 2 and 3) in a previously introduced format,<sup>30</sup> whereby visual inspection of simulation trajectories is accompanied by molecular distribution histograms to understand mixing, force development curves in the direction of the indentation, and measurements of the length of the connective neck formed between the two objects. This study also

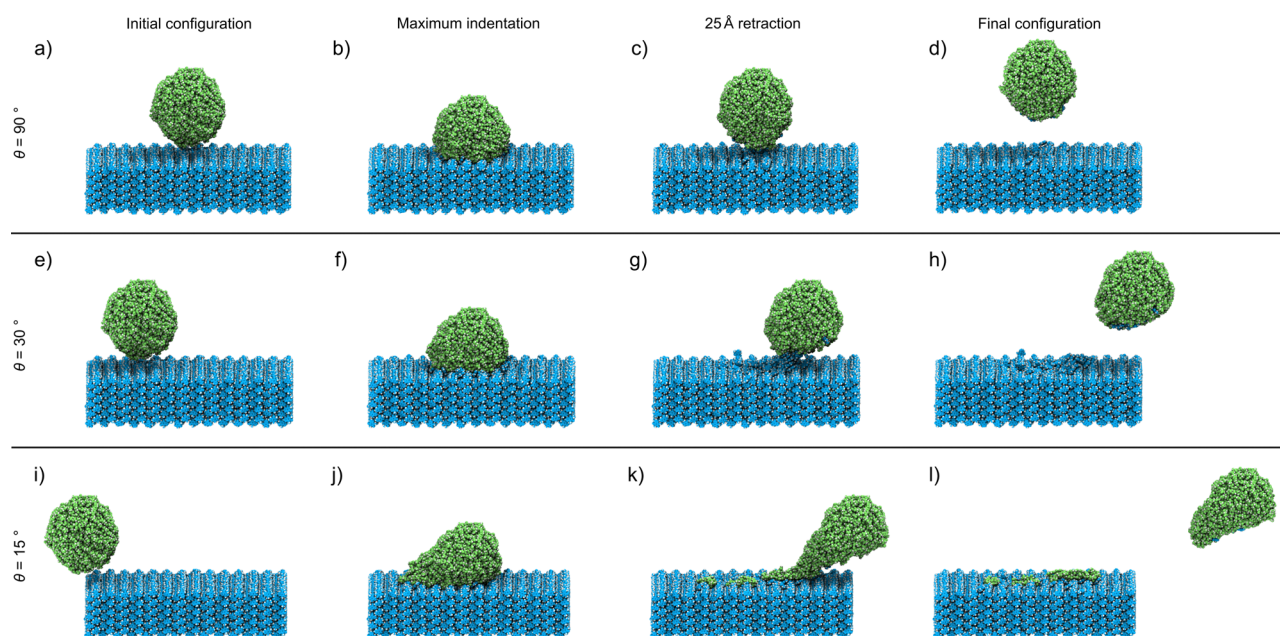


**Fig. 2** Snapshots of the simulated indentation of the **cit** nanoparticle (green) on a slab of **theo** (blue) with the (001) surface exposed, where the nanoparticle travels at  $8 \text{ m s}^{-1}$  and incident angles of (a–d)  $90^\circ$ , (e–h)  $30^\circ$ , (i–l) and  $15^\circ$ . The snapshots show (a, e and i) the initial configuration, (b, f and j) the point of maximum indentation, (c, g and k) after retraction of the nanoparticle by 25 Å, and (d, h and l) the final configuration after retraction by 50 Å for each simulated indentation process.





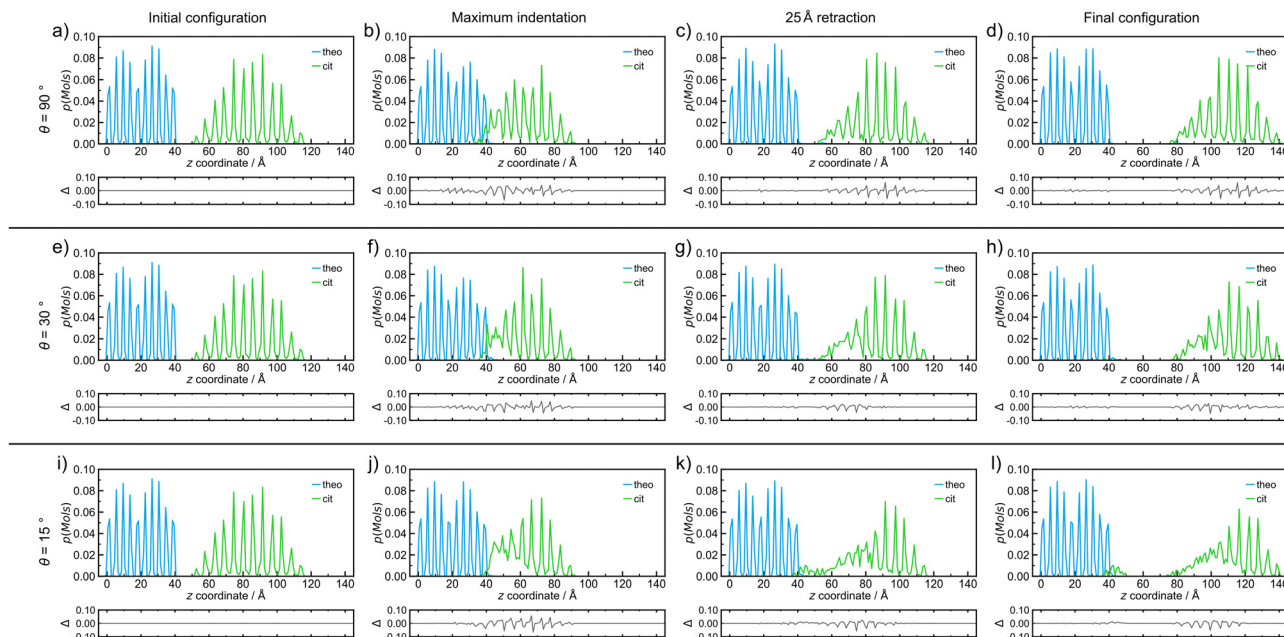


**Fig. 3** Probability density distributions of molecules of each species, **theo** (blue) and **cit** (green), for simulated indentations where the nanoparticle travels at  $8 \text{ m s}^{-1}$  and incident angles of (a–d)  $90^\circ$ , (e–h)  $30^\circ$ , and (i–l)  $15^\circ$ . The plot distributions when at (a, e and i) the initial configuration, (b, f and j) the point of maximum indentation, (c, g and k) after retraction of the nanoparticle by  $25 \text{ \AA}$ , and (d, h and l) the final configuration after retraction of  $50 \text{ \AA}$  for each simulated indentation process. The probability density distributions in this figure correspond directly to the simulation snapshots shown in Fig. 2. Below each distribution, a difference curve is given, which highlights the changes relative to the initial configuration.

incorporates an analysis of the structural deformation suffered by the nanoparticle by determining the changes in sphericity. In this study, we started with the simulation of direct indentations, where  $\theta = 90^\circ$ . Visual inspection allows us to observe the key points of the indentation process (Fig. 2(a)–(d)), with the indentation speed set at  $8 \text{ m s}^{-1}$  in this case. The simulation process is best described through forward indentation and subsequent retraction stages, corresponding to the processes in which the **cit** nanoparticle impacts and disrupts the **theo** surface, and processes in which the nanoparticle is being dragged out of the **theo** surface, respectively. These are illustrated by visual inspection of several key points of the experiment at which  $\theta = 90^\circ$  and the speed along  $v$  is  $8 \text{ m s}^{-1}$  (Fig. 2(a)–(d)).<sup>‡</sup> The first key point corresponds to the starting configuration, in which the **cit** particle (green) is situated  $5 \text{ \AA}$  above the centre of the **theo** (001) slab surface (blue) (Fig. 2(a)). The next key point (Fig. 2(b)) corresponds to the configuration at the maximum indentation of the **cit** particle into the surface, when the nanoparticle is indented on the surface by  $20 \text{ \AA}$ . In the retraction stage, the key points for analysis are when **cit** has been retracted by  $25 \text{ \AA}$  (Fig. 2(c)), *i.e.* when the molecules with fixed trajectories have the same separation from the slab in  $z$  as found in the starting position, and the final point of the simulation where the **cit** nanoparticle has been retracted by a

total of  $50 \text{ \AA}$  (Fig. 2(d)). While visually there does not appear to have been any transfer of molecules between the two materials, there is, in fact, a small number (13) of **theo** molecules that have been abstracted from the slab by the nanoparticle. This represents approximately  $0.3\%$  of the 4098 molecules, of both **cit** and **theo**, that were free to move in the simulation.

Since molecular mixing, especially if low fractions of molecules are involved, might be difficult to detect and quantify by visual inspection, the analysis of molecular mixing and transfer is best performed by tracking the centre of mass for all molecules in the system, followed by determining the number of molecules of **theo** and **cit**, whose  $z$ -coordinates were above and below  $55 \text{ \AA}$  in the final configuration, respectively. The corresponding histogram plots of the molecular distributions along the  $z$ -axis (Fig. 3(a)–(d)) show two well-defined regions of the population with regularly spaced maxima for the initial configuration (Fig. 3(a)), which is expected due to the regular packing of molecules in the parent crystal structures. At the point of maximum indentation, the histogram corresponding to **cit** (green) exhibits a small amount of compression of  $\approx 5 \text{ \AA}$  (Fig. 3(b)), which is a result of the nanoparticle being distorted upon being pressed into the **theo** slab. In the middle of the retraction step, a trace of **theo** (blue) can be observed occupying the same region as the **cit**, demonstrating molecular mixing. The lack of a probability density for either species in the range of  $45 \text{ \AA}$  to  $50 \text{ \AA}$  at this stage signifies that the two objects have been separated. The probability density histograms for the final configuration (Fig. 3(d)) are very similar to those of the previous stage, with the only perceivable difference being the larger

<sup>‡</sup> All simulation snapshots presented herein were visualised with VMD v1.9.4a55<sup>44</sup> and rendered with Tachyon, v0.99.<sup>45</sup> All atomic positions have been unwrapped from the periodic boundary conditions, and hydrogen atoms are rendered in white throughout for visualisation purposes.



separation between the two objects. The molecular transfer values were consistently low for all four of the indentation speeds investigated in this work and were almost 30 times lower than those observed for indentations between two nanoparticles in 2019.<sup>30</sup> This is caused by two factors: (I) the surface of the pristine is free of defects and, consequently, molecules at the surface will be less mobile than those at a high curvature surface, such as the surface of previously studied nanoparticles,<sup>30</sup> and (II) the large size of the **theo** slab, required for the simulations, results in large regions of **theo** molecules that are not involved in the indentation process, reducing the transfer percentage significantly. It was previously established that the interaction of organic nanoparticles, with or without the presence of liquid additives, leads to the formation of a connective neck, which is a small region of particles that maintains all of the particles in the simulation as a single object when the retraction process exceeds 20 Å (where the surface of **theo** terminates). The formation of a connective neck, which enables extensive intermolecular mixing, is likely to be a critical aspect of mechanochemical cocrystallisation and reactions of molecular materials. In this case ( $\theta = 90^\circ$ , speed along  $\nu$  was  $8 \text{ m s}^{-1}$ ), there was no evidence of connective neck formation (Fig. 2(c) and 3(c)), which is suggested to play a role in the molecular transfer process in mechanochemical indentations.<sup>36</sup> However, at indentation speeds of  $4 \text{ m s}^{-1}$  to  $1 \text{ m s}^{-1}$ , small short-lived connective necks were observed (Fig. S4 and S5 (ESI<sup>†</sup>), respectively), further suggesting that surface molecules on the **theo** surface are less prone to leaving the surface than were observed for indentations of two nanoparticles.<sup>36</sup> Full details on the tracking and evaluations of molecular transfer and connective neck analyses are provided in Sections S2 and S3 (ESI<sup>†</sup>). Additionally, the results described here are clearly shown in the renders of the simulation trajectories supplied in the ESI<sup>†</sup>.

Reducing the incident angle  $\theta$  to  $75^\circ$  leads to the formation of small 0.8 nm to 2.0 nm, short-lived (0.05 ns to 2.05 ns) connective necks between the nanoparticle and the slab during the retraction stage (Fig. S6–S9, ESI<sup>†</sup>). In this case, a connective neck was observed and measured (Table S4, ESI<sup>†</sup>) for each of the four speeds investigated, which is believed to be a key feature that facilitates molecular transfer during simulated indentations.<sup>36</sup> However, the percentage of molecules transferred during the indentation remained comparable to indentations with  $\theta = 90^\circ$ , suggesting that the formation of a connective neck is not the sole indicator of improved transfer between molecular species. Additionally, there again appears to be little or no disruption to the geometry of the nanoparticle. Further decreasing  $\theta$ , *i.e.* when the indentation becomes increasingly indirect, results in a much more pronounced formation of connective necks between the two indenting objects. Additionally, the simulation also reveals a greater degree of disruption to both the **theo** surface and the **cit** nanoparticle. This is most evident for indentations conducted at the lowest  $\theta$  values used in this work ( $30^\circ$  and  $15^\circ$ ). Snapshots of an indentation with an indentation speed of  $8 \text{ m s}^{-1}$  and  $\theta = 30^\circ$  (Fig. 3(e)–(h)) and  $\theta = 15^\circ$  (Fig. 3(i)–(l)) show the extent of

the changes to the simulated indentation process. First, the extent of displacement  $x$  applied to the **cit** nanoparticle is observed to create the initial configurations (Fig. 3(e) and (i)). Again, at the point of maximum indentation, there is a noticeable compression in the distribution of **cit** molecules (Fig. 3(b) and (f)). In fact, for indentations where  $\theta = 15^\circ$ , the distribution is compressed by a further  $\approx 5 \text{ Å}$  when compared to indentations at  $90^\circ$ . This change is not caused by the increased force during indentation, as the force development analysis reveals a decrease in the maximum force experienced as  $\theta$  decreases (Section S5, ESI<sup>†</sup>). Instead, this is due to the **cit** molecules being dragged across the surface of the slab; therefore, the molecules are being spread out in the  $xy$  plane, which can be seen in Fig. 2(j). After being retracted by 25 Å (Fig. 3(g) and (k)), a significant connective neck formed between the two materials in both cases. When  $\theta = 30^\circ$ , the connective neck appears to be formed predominantly by **theo** molecules (Fig. 2(g)), which is confirmed by molecular distribution analysis (Fig. 3(g)). However, when  $\theta$  is reduced to  $15^\circ$ , the connective neck consists of predominantly **cit** molecules (Fig. 2 and 3(k)). This change in composition is likely not dependent on the angle and is more likely to be an effect of the initial conditions of each simulation. The transfer of **cit** molecules (green) to the **theo** surface (blue) is also visible when  $\theta = 15^\circ$  (Fig. 3(k)), with molecules of **cit** deposited upon the **theo** slab evident upon the separation of the objects (Fig. 3(l)). For the indentation where  $\theta = 30^\circ$ , a small number of **theo** and **cit** molecules were transferred between the two objects (Fig. 3(h)). In the case when  $\theta = 15^\circ$ , a clear number of **cit** molecules were deposited on the **theo** surface. In this case, a total of 45 molecules were transferred during the indentation. While still a low percentage of free molecules ( $\approx 1.0\%$ ), this is a three-fold increase in molecular transfer when compared to a direct collision. The values of molecular transfer for all simulated indentations (Table 1) show that the number of molecules transferred during indentations between **cit** and **theo** is generally low. However, the numbers suggest that decreasing  $\theta$  improves the transfer process between the particles. Generally,  $\theta$  values of  $15^\circ$  or  $30^\circ$  result in a greater amount of molecules being transferred during indentation. A more in-depth analysis of the trends in molecular transfer would require multiple, different initial configurations for the **cit** nanoparticle for each indentation trajectory, *i.e.* for all indentation speeds and  $\theta$ , which is beyond the scope of the current work.

**Table 1** Total number of molecules transferred between **cit** and **theo** for simulated indentations over a range of indentation speeds ( $161 \text{ m s}^{-1}$ ) and angles ( $\theta = 90^\circ$  to  $15^\circ$ )

	$\theta/^\circ$					
	90	75	60	45	30	15
Speed/ $\text{m s}^{-1}$	Molecules transferred					
16	6	8	9	3	12	28
8	13	3	7	12	18	45
4	5	1	9	8	14	12
1	4	8	5	3	4	53



**Table 2** Percentage changes in sphericity ( $\Delta\% \Psi$ ) of the **cit** nanoparticle after simulated indentations over a range of indentation speeds ( $161 \text{ m s}^{-1}$ ) and angles ( $\theta = 90^\circ$  to  $15^\circ$ )

Speed/ $\text{m s}^{-1}$	$\theta/^\circ$					
	90	75	60	45	30	15
	$\Delta\% \Psi/\%$					
16	-1.3	-1.4	-1.2	-1.6	-3.6	-4.7
8	-1.1	-1.7	-1.9	-2.4	-2.8	-5.9
4	-2.2	-1.5	-2.5	-1.8	-4.3	-3.8
1	-1.4	-0.9	-4.8	-1.9	-3.2	-8.4

More noticeable than the **cit** molecules on the **theo** surface (Fig. 3(d)), is the significant disruption of the **cit** nanoparticle as a result of the indentation, which in this case resembles an irregular ovoid rather than a sphere. To measure this disruption, we calculated the change in the sphericity of the particles for each simulated indentation. Sphericity was calculated using Waddell's sphericity index<sup>46</sup> ( $\Psi$ ),

$$\Psi = \frac{S_{\text{ideal}}}{S} \quad (1)$$

where  $S$  is the measured surface area of the particle,  $S_{\text{ideal}}$  is the surface area of a perfect sphere with a volume equal to that of the measured particle, and  $\Psi = 1$  corresponds to a perfect sphere. The surface area and volume of the **cit** nanoparticle were obtained using the surface mesh construction method in the Ovito<sup>47</sup> code, v2.9, with a probe radius of  $3.0 \text{ \AA}$  and a smoothing level of 10. The sphericity index of the nanoparticle before indentation ( $\Psi_0$ ) was 0.9 and was used as the reference point from which the percentage changes in sphericity ( $\Delta\% \Psi$ ) were calculated (Table 2). The data shows that the indentation consistently caused a decrease in sphericity for all indentation trajectories in the study. Again, it is evident that lower  $\theta$  values, especially  $15^\circ$  or  $30^\circ$ , result in the most significant changes in the system, with  $\Delta\% \Psi$  decreases that are two to four times greater than those for more direct indentations, where  $\theta = 75^\circ$  or  $90^\circ$ . Similar to the observations in molecular transfer, indentations where  $\theta = 45^\circ$  to  $60^\circ$  exhibit a high degree of variability for the change in the sphericity of the nanoparticle. In some cases, they are closer to more direct indentations, and in others, they are more similar to the indentations at lower  $\theta$  values. To fully understand these trends, a substantial quantity of unique initial configurations was required. The analysis of molecular transfer and sphericity do not show a definite effect on the indentation speed. While the largest number of molecules transferred and the greatest decrease in sphericity were observed for the lowest speeds and  $\theta$ , *i.e.*  $1 \text{ m s}^{-1}$  and  $15^\circ$ , the values observed when the indentation speed was  $8 \text{ m s}^{-1}$  for the same  $\theta$  were not dissimilar. Overall, MD simulations indicate that  $\theta$  plays the most important role in molecular transfer and the degree of disruption to the nanoparticle, which can be ascribed to two intertwined effects. At lower  $\theta$  values, the molecules of **cit** are brought into contact with more molecules of the **theo** slab as the initial and final points of contact move further from the centre of the  $xy$  plane of the slab as

$\theta$  decreases. This results in greater contact time between the two species. In fact, indentations at  $\theta = 30^\circ$  or  $15^\circ$  take approximately two and four times longer to occur, respectively, than those at  $\theta = 90^\circ$  and  $75^\circ$ . In particular, the indentations at  $\theta = 15^\circ$  are twice as long as those at  $\theta = 30^\circ$ , which is the largest increase in time between any two consecutive angles in this study. Therefore, with a greater number of potential contacts between molecules of different species and more time for the molecules to move and reorganise themselves, there is a greater tendency for molecular transfer. In addition, a decrease in  $\theta$  leads to a greater level of structural disruption to the **cit** nanoparticle, which is observed by the decrease in sphericity of the particle itself and in the length of the connective neck formed with the **theo** slab. While the increased disruption is linked to the increase in molecular transfer, we believe that this disruption will play a much greater role in subsequent mechanochemical events, as the disruption will result in higher energy surfaces, which facilitates molecular transfer.

## Conclusions

This study has focused on the use of theoretical methods to understand the effects of mechanical interactions on the structural disruption and transfer of molecules between organic molecular solids that are known to form a cocrystal by ball milling.<sup>31</sup> Classical force field MD was employed to investigate how the angle of incidence and indentation speed play important roles in simulated mechanochemical indentations of a nanoparticle of citric acid on a slab of theophylline, two crystalline molecular solids of pharmaceutical interest. The results indicate that the angle of incidence, ranging from  $90^\circ$  or  $75^\circ$  for more direct indentations to  $30^\circ$  or  $15^\circ$  for more grazing indentations, has a significant and profound effect on the indentation outcome. First, the amount of material transferred between the two materials significantly increased at a lower value of  $\theta$ . This occurs because a larger number of molecules are in contact with each other for a greater amount of time, increasing the chances of transfer occurring upon retraction. Second, the degree of disruption to the initially spherical nanoparticle is up to four times greater for more grazing angles of incidence when compared to more direct indentations. Reducing the speed of the incident nanoparticles promotes the formation of connective necks between citric acid and theophylline, which elongate as the speed is further reduced. However, this effect did not directly translate into a discernible trend in either molecular transfer or disruption of the nanoparticles. Although experimentally reactions do not necessarily occur at specified angles or speeds, this work suggests that lower angles of incidence between two particles are the most effective in the early stages of a mechanochemical reaction, regardless of their incident speeds. While considerable effort has been focused on the theoretical modelling of mechanochemistry in the context of rearrangements of covalent bonds,<sup>26–28</sup> less attention has been dedicated to another aspect of mechanochemistry that typically precedes covalent



transformations in organic solids: the mechanically induced rearrangement of molecules and the disruption of the supramolecular structure. We hope that the work presented herein will inspire future studies in this direction, aiming towards an integrated understanding of mechanochemical processes at the molecular and supramolecular levels.

## Author contributions

M. F.: (invited) conceptualization, investigation, data curation, formal analysis, visualization, writing – original draft, review & editing; T. F.: conceptualization, supervision, resources, writing – review & editing.

## Conflicts of interest

There are no conflicts to declare.

## Acknowledgements

We thank support from the Leverhulme International Professorship (TF) and the University of Birmingham. Calculations were performed using the University of Birmingham's Blue-BEAR HPC service and the Sulis Tier 2 HPC platform hosted by the Scientific Computing Research Technology Platform at the University of Warwick. Sulis is funded by EPSRC grant EP/T022108/1 and the HPC Midlands+ consortium. We also thank Prof. A. J. Morris for fruitful discussions during the development of this work.

## Notes and references

- (a) S. L. James, C. J. Adams, C. Bolm, D. Braga, P. Collier, T. Friščić, F. Grepioni, K. D. M. Harris, G. Hyett, W. Jones, A. Krebs, J. Mack, L. Maini, A. G. Orpen, I. P. Parkin, W. C. Shearouse, J. W. Steed and D. C. Waddell, *Chem. Soc. Rev.*, 2012, **41**, 413–447; (b) T. Friščić, C. Mottillo and H. M. Titi, *Angew. Chem., Int. Ed.*, 2020, **59**, 1018–1029; (c) A. A. L. Michalchuk, E. V. Boldyreva, A. M. Belenguer, F. Emmerling and V. V. Boldyrev, *Front. Chem.*, 2021, **9**, 685789.
- T. Seo, N. Toyoshima, K. Kubota and H. Ito, *J. Am. Chem. Soc.*, 2021, **143**, 6165–6175.
- Y. X. Shi, K. Xu, J. K. Clegg, R. Ganguly, H. Hirao, T. Friščić and F. García, *Angew. Chem., Int. Ed.*, 2016, **55**, 12736–12740.
- (a) H. M. Titi, J.-L. Do, A. J. Howarth, K. Nagapudi and T. Friščić, *Chem. Sci.*, 2020, **11**, 7578–7584; (b) L. Gonnet, C. B. Lennox, J.-L. Do, I. Malvestiti, S. G. Koenig, K. Nagapudi and T. Friščić, *Angew. Chem., Int. Ed.*, 2022, **61**, e202115030.
- D. E. Crawford and J. Casaban, *Adv. Mater.*, 2016, **28**, 5747–5754.
- D. Hasa and W. Jones, *Adv. Drug Delivery Rev.*, 2017, **117**, 147–161.
- C. Medina, D. Daurio, K. Nagapudi and F. Alvarez-Nunez, *J. Pharm. Sci.*, 2010, **99**, 1693–1696.
- K. Nagapudi, E. Y. Umanzor and C. Masui, *Int. J. Pharm.*, 2017, **521**, 337–345.
- (a) D. Braga, S. L. Giaffreda, F. Grepioni, M. R. Chierotti, R. Gobetto, G. Palladino and M. Polito, *CrystEngComm*, 2007, **9**, 879–881; (b) D. Braga, F. Grepioni, L. Maini, S. Prosperi, R. Gobetto and M. R. Chierotti, *Chem. Commun.*, 2010, **46**, 7715–7717; (c) M. J. Cliffe, C. Mottillo, R. S. Stein, D.-K. Bučar and T. Friščić, *Chem. Sci.*, 2012, **3**, 2495–2500.
- A. J. Stirk, F. E. S. Souza, J. Gerster, F. M. Mir, A. Karadeolian and A. W. Rey, *Green Chem.*, 2022, **24**, 1505–1514.
- P. Lavalle, F. Boulmedais, P. Schaaf and L. Jierry, *Langmuir*, 2016, **32**, 7265–7276.
- J. B. Kelber, A. Bensalah-Ledoux, S. Zahouani, B. Baguenard, P. Schaaf, A. Chaumont, S. Guy and L. Jierry, *Angew. Chem., Int. Ed.*, 2020, **59**, 23283–23290.
- A. A. L. Michalchuk, in *Mechanochemistry and emerging technologies for sustainable chemical manufacturing*, ed. E. Colacino and F. Garcia, CRC Press, London, England, 2023, ch. 3, pp. 60–83.
- I. Halasz, S. A. J. Kimber, P. J. Beldon, A. M. Belenguer, F. Adams, V. Honkimäki, R. C. Nightingale, R. E. Dinnebier and T. Friščić, *Nat. Protoc.*, 2013, **8**, 1718–1729.
- D. Gracin, V. Štrukil, T. Friščić, I. Halasz and K. Užarević, *Angew. Chem., Int. Ed.*, 2014, **53**, 6193–6197.
- L. Batzdorf, F. Fischer, M. Wilke, K.-J. Wenzel and F. Emmerling, *Angew. Chem., Int. Ed.*, 2015, **54**, 1799–1802.
- P. F. M. de Oliveira, A. A. L. Michalchuk, A. G. Buzanich, R. Bienert, R. M. Torresi, P. H. C. Camargo and F. Emmerling, *Chem. Commun.*, 2020, **56**, 10329–10332.
- P. A. Julien, M. Arhangelskis, L. S. Germann, M. Etter, R. E. Dinnebier, A. J. Morris and T. Friščić, *Chem. Sci.*, 2023, **14**, 12121–12132.
- J. G. Schiffmann, F. Emmerling, I. C. Martins and L. Van Wüllen, *Solid State Nucl. Magn. Reson.*, 2020, **109**, 101687.
- C. Leroy, S. Mittlelette, G. Félix, N. Fabregue, J. Špačková, P. Gaveau, T.-X. Métro and D. Laurencin, *Chem. Sci.*, 2022, **13**, 6328–6334.
- P. Chattopadhyay, I. Manna, S. Talapatra and S. Pabi, *Mater. Chem. Phys.*, 2001, **68**, 85–94.
- M. Broseghini, M. D'Incau, L. Gelisio, N. Pugno and P. Scardi, *Mater. Des.*, 2016, **110**, 365–374.
- L. Yang, A. Moores, T. Friščić and N. Provatas, *ACS Appl. Nano Mater.*, 2021, **4**, 1886–1897.
- M. Carta, F. Delogu and A. Porcheddu, *Phys. Chem. Chem. Phys.*, 2021, **23**, 14178–14194.
- M. Carta, L. Vugrin, G. Miletic, M. J. Kulcsár, P. C. Ricci, I. Halasz and F. Delogu, *Angew. Chem., Int. Ed.*, 2023, **62**, e202308046.
- J. Ribas-Arino and D. Marx, *Chem. Rev.*, 2012, **112**, 5412–5487.
- Y. S. Zholdassov, L. Yuan, S. R. Garcia, R. W. Kwok, A. Boscoboinik, D. J. Valles, M. Marianski, A. Martini, R. W. Carpick and A. B. Braunschweig, *Science*, 2023, **380**, 1053–1058.





- 28 A. A. L. Michalchuk, *Faraday Discuss.*, 2023, **241**, 230–249.
- 29 (a) K. Mohammadtabar, S. J. Eder, N. Dörr and A. Martini, *Tribol. Int.*, 2022, **176**, 107922; (b) F. H. Bhuiyan, S. H. Kim and A. Martini, *Appl. Surf. Sci.*, 2022, **591**, 153209.
- 30 M. Ferguson, M. S. Moyano, G. A. Tribello, D. E. Crawford, E. M. Bringa, S. L. James, J. Kohanoff and M. G. Del Pópolo, *Chem. Sci.*, 2019, **10**, 2924–2929.
- 31 S. Karki, T. Frišćić, W. Jones and W. D. S. Motherwell, *Mol. Pharmaceutics*, 2007, **4**, 347–354.
- 32 S. Plimpton, *J. Comput. Phys.*, 1995, **117**, 1–19.
- 33 (a) W. L. Jorgensen and J. Tirado-Rives, *J. Am. Chem. Soc.*, 1988, **110**, 1657–1666; (b) W. L. Jorgensen, D. S. Maxwell and J. Tirado-Rives, *J. Am. Chem. Soc.*, 1996, **118**, 11225–11236.
- 34 J. E. Lennard-Jones, *Proc. Phys. Soc.*, 1931, **43**, 461.
- 35 S. L. Mayo, B. D. Olafson and W. A. Goddard, *J. Phys. Chem.*, 1990, **94**, 8897–8909.
- 36 R. Hockney and J. Eastwood, *Computer Simulation Using Particles*, Taylor & Francis, New York, 1998.
- 37 S. J. Clark, M. D. Segall, C. J. Pickard, P. J. Hasnip, M. I. J. Probert, K. Refson and M. C. Payne, *Z. Kristallogr. Cryst. Mater.*, 2005, **220**, 567–570.
- 38 C. R. Groom, I. J. Bruno, M. P. Lightfoot and S. C. Ward, *Acta Crystallogr., Sect. B: Struct. Sci., Cryst. Eng. Mater.*, 2016, **72**, 171–179.
- 39 J. P. Glusker, J. A. Minkin and A. L. Patterson, *Acta Crystallogr., Sect. B: Struct. Sci., Cryst. Eng. Mater.*, 1969, **25**, 1066–1072.
- 40 Y. Ebisuzaki, P. D. Boyle and J. A. Smith, *Acta Crystallogr., Sect. C: Struct., Chem.*, 1997, **53**, 777–779.
- 41 U. Landman, W. Luedtke and E. M. Ringer, *Wear*, 1992, **153**, 3–30.
- 42 F. Delogu, M. Monagheddu, G. Mulas, L. Schiffini and G. Cocco, *J. Non-Cryst. Solids*, 1998, **232–234**, 383–389.
- 43 K. Linberg, P. Szymoniak, A. Schönhals, F. Emmerling and A. A. L. Michalchuk, *Chem. – Eur. J.*, 2023, e202302150.
- 44 W. Humphrey, A. Dalke and K. Schulten, *J. Mol. Graph.*, 1996, **14**, 33–38.
- 45 J. E. Stone, MSc thesis, University of Missouri-Rolla, MO, USA, 1996.
- 46 H. Wadell, *J. Geol.*, 1932, **40**, 443–451.
- 47 A. Stukowski, *Modell. Simul. Mater. Sci. Eng.*, 2010, **18**, 015012.

